RESEARCH ARTICLE
SOLID EARTH: SEISMOLOGY

Earth and Planetary Physics
8: 522–534, 2024
doi: 10.26464/epp2024019

The 2023 M_W 6.8 Adassil Earthquake (Chichaoua, Morocco) on a steep reverse fault in the deep crust and its geodynamic implications

Billel Touati[1†], WangWang Gu[2,3*†], SiDao Ni[1,2,3], Risheng Chu[2,3], MinHan Sheng[2,3], QingJie Xue[1], Fouzi Bellalem[4], Said Maouche[4], and Habibi Yahyaoui[5]

[1]School of Earth and Space Sciences, University of Science and Technology of China, Hefei 230026, China;

[2]State Key Laboratory of Geodesy and Earth's Dynamics, Innovation Academy for Precision Measurement Science and Technology, Chinese Academy of Sciences, Wuhan 430077, China;

[3]College of Earth and Planetary Sciences, University of Chinese Academy of Sciences, Beijing 100049, China;

[4]Centre de Recherche en Astronomie, Astrophysique et Géophysique (CRAAG), BP 63, Bouzaréah, Algiers 16340, Algeria;

[5]Geography and Territory Planning, Natural Hazards and Territory Planning Laboratory, Batna 2 University, Fesdis, Batna 05000, Algeria

Key Points:

- The 2023 Adassil earthquake in the High Atlas offered a rare opportunity to study deep crustal seismicity mechanics.
- Analysis of seismic waves and InSAR data revealed a reverse fault mechanism with a centroid depth of approximately 28 km, exceeding typical seismogenic thickness.
- Geological factors, such as cooler temperatures in the lower crust and the region's volcanic legacy, contribute to stress accumulation and seismic rupture, highlighting the need for enhanced research and surveillance in similar geological settings.

Citation: Touati, B., Gu, W. W., Ni, S. D., Chu, R., Sheng, M. H., Xue, Q. J., Bellalem, F., Maouche, S., and Yahiaoui, H. (2024). The 2023 M_W 6.8 Adassil Earthquake (Chichaoua, Morocco) on a steep reverse fault in the deep crust and its geodynamic implications. *Earth Planet. Phys.*, *8*(3), 522–534. http://doi.org/10.26464/epp2024019

Abstract: The M_W 6.8 Adassil earthquake that occurred in the High Atlas on September 8, 2023, was a catastrophic event that provided a rare opportunity to study the mechanics of deep crustal seismicity. This research aimed to decipher the rupture characteristics of the Adassil earthquake by analyzing teleseismic waveform data in conjunction with interferometric synthetic aperture radar (InSAR) observations from both ascending and descending orbits. Our analysis revealed a reverse fault mechanism with a centroid depth of approximately 28 km, exceeding the typical range for crustal earthquakes. This result suggests the presence of cooler temperatures in the lower crust, which facilitates the accumulation of tectonic stress. The earthquake exhibited a steep reverse mechanism, dipping at 70°, accompanied by minor strike-slip motion. Within the geotectonic framework of the High Atlas, known for its volcanic legacy and resulting thermal irregularities, we investigated the potential contributions of these factors to the initiation of the Adassil earthquake. Deep seismicity within the lower crust, away from plate boundaries, calls for extensive research to elucidate its implications for regional seismic hazard assessment. Our findings highlight the critical importance of studying and preparing for significant seismic events in similar geological settings, which would provide valuable insights into regional seismic hazard assessments and geodynamic paradigms.

Keywords: Adassil earthquake; seismogenic fault; source depth; interferometric synthetic aperture radar (InSAR); seismic waveform; joint inversion

1. Introduction

On September 8, 2023, an earthquake of magnitude 6.8 occurred near the town of Adassil in the High Atlas Mountains, Al Haouz Province, Morocco, hereafter referred to as the Adassil earthquake. The earthquake epicenter was located at 31.058°N and 8.490°W, with a focal depth of 26 km according to the Euro-Mediterranean Seismological Centre and 27.8 km according to the Global Centroid Moment Tensor (CMT) Project. The Adassil earthquake led to an estimated 3000 fatalities, leaving many victims unaccounted for and hundreds with varying degrees of physical injuries. The historic city of Marrakech and various isolated communities in the Atlas Mountains suffered significant destruction from the Adassil earthquake (Peláez, 2023). Considered one of the most devastating earthquakes in the High Atlas region, the Adassil earthquake was followed by a series of aftershocks; one substantial event with a magnitude of M_s 4.9 occurred approximately 20 min later and was situated approximately 5 km from

First author: B. Touati, billeltouati@mail.ustc.edu.cn
Correspondence to: W. W. Gu, guww@apm.ac.cn
† These authors contributed equally to this work.
Received 30 NOV 2023; Accepted 18 FEB 2024.
First Published online 15 MAR 2024.

the epicenter of the mainshock (Figure 1). This event occurred in the proximity of the North Atlas fault zone (Levandowski, 2023), where the occurrence of moderate to large earthquakes within a 500-km radius has been relatively low, based on U.S. Geological Survey (USGS) records dating back to 1900 (Yeck et al., 2023). Because of its substantial intensity and relatively low frequency, the 2023 Adassil earthquake presents the opportunity for a unique case study of deep crustal earthquakes.

Along the Atlantic coast of Morocco, the seismicity rate is significantly elevated because of the subduction process associated with the convergence of the African and Eurasian Plates (Cherkaoui and El Hassani, 2012). In contrast to these subduction-zone earthquakes, shallow intraplate earthquakes on the Morocco arc, located far from the trench, are rare, especially for events with a moment magnitude (M_w) above 5.0 (Figure 1). However, according to the USGS catalog, earthquakes in this area exhibit a wide range of depths. Most earthquakes are confined to depths within 30 km, but some extend beyond 40 km (Cherkaoui and El Hassani, 2012). Gosset (2004) indicated a Moho depth of approximately 30–35 km in this region. This finding implies that some earthquakes occur within the lower crust or even in the mantle, deviating from the depths typically associated with tectonic earthquakes. Furthermore, the lower crust and mantle rocks are characterized by higher temperatures, rendering brittle deformation less likely. These data suggest that the tectonic setting of the region remains enigmatic. Accurate determination of source parameters is crucial for a comprehensive understanding of the seismotectonic environment surrounding the Adassil earthquake and its associated hazards. The centroid depth, for example, often correlates with the primary slip distribution of an earthquake and can provide insights into the rupture processes and seismogenic context (Maggi et al., 2000).

Previous studies have outlined the complex faulting mechanisms of the Adassil earthquake and the challenges in attributing seismic activity to known structures in the region (Levandowski, 2023; Yeck et al., 2023). These studies have highlighted regional crustal stress and slip potential, emphasizing north–south shortening with various fault orientations. The anomalously hot lower crust in the Western High Atlas influences fault stability. Yeck et al. (2023) integrated seismic and geodetic data, which revealed oblique-reverse faulting in the lower crust with a compact source and a centroid depth challenging conventional estimates. Typically, the temperature gradually increases with depth in the Earth's crust. However, it is important to highlight that specific regions demonstrate relatively lower temperatures within the crust. This unique thermal condition can contribute to the occurrence of moderately intense seismic activities in the lower crust. Noteworthy instances illustrating this phenomenon include the M_w 7.7 Bhuj earthquake in 2021 (Mandal et al., 2004), the M_w 5.2 Chifeng earthquake in 2009 (Wei SJ et al., 2009), and the M_w 6.6 Hokkaido earthquake in 2018 (Zang C et al., 2019). In light of the significant magnitude of the Adassil earthquake, which caused noticeable surface deformation, as recorded by ascending and descending orbiting satellites, we use interferometric synthetic aperture radar (InSAR) data to constrain the 2023 earthquake fault. To gain insights into the

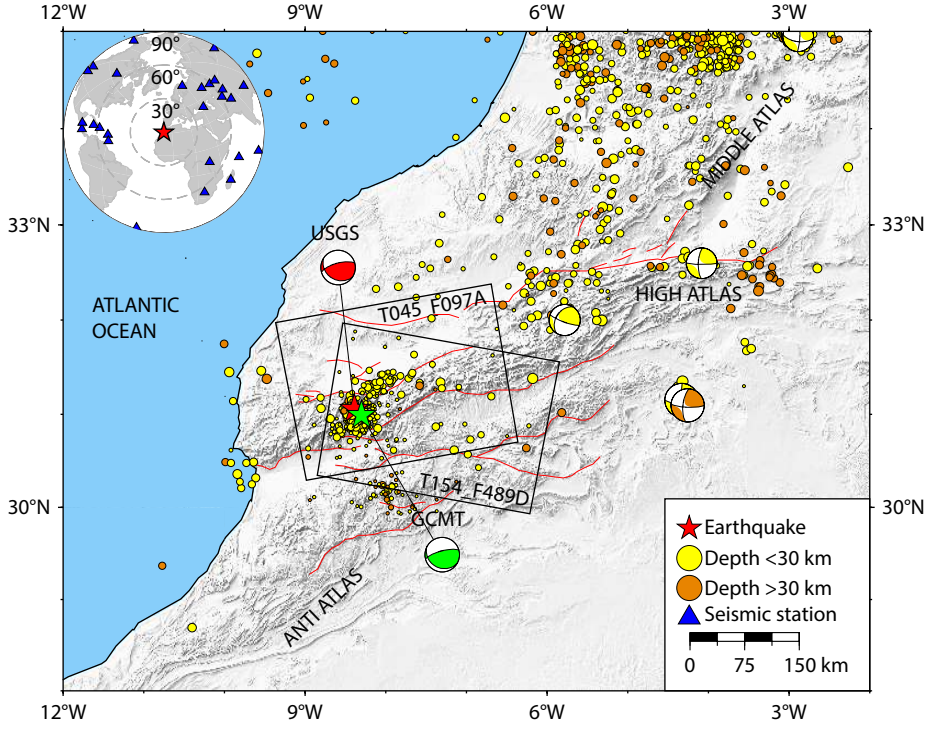

Figure 1. The seismotectonic setting of the 2023 Adassil earthquake. The earthquake epicenter, situated in the High Atlas region, is marked by a red star, accompanied by some aftershocks. The beachball diagram, featuring various colors, illustrates the seismic mechanism based on data from the USGS and the Global CMT (GCMT) catalog. The yellow dots represent earthquake depths less than 30 km, whereas the orange dots indicate depths greater than 30 km. The extent of the Sentinel-1 image is outlined by a black rectangle. The blue triangles denote teleseismic stations (30°–90°) utilized in the inversion process. Active faults are highlighted by a red line.

broader implications of deep-seated earthquakes for surface deformation, it is pertinent to reference notable instances such as the strong M_w 8.0 earthquake in Peru in 2019, recognized as the deepest seismic event analyzed with InSAR (Vallée et al., 2023). Additionally, the M_w 6.4 Taiwan Meinong earthquake in 2016 (Huang MH et al., 2016; Yang YH et al., 2021) and the M_w 7.3 Sarpol-e Zahab (Iran) earthquake in 2017 (Vajedian et al., 2018) underscore the impact of seismic occurrences originating from substantial depths across diverse tectonic settings. The study of these cases has contributed to a holistic comprehension of seismicity, emphasizing the imperative nature of investigating deep crustal earthquakes.

In addition to the depth of the source, the focal mechanism is a critical parameter for analyzing earthquake initiation mechanisms (Chu RS and Sheng MH, 2023). Focal mechanism solutions from the USGS and Global CMT indicate that the earthquake occurred on a southeast-dipping reverse fault and a southwest-dipping high-angle reverse fault, respectively. The focal mechanism alone cannot distinguish between the causative fault and its auxiliary. Therefore, further determination of the causative fault for this earthquake requires the integration of additional methods, such as surface rupture field surveys (Xu XW et al., 2008), the spatial distribution of aftershocks (Zhang HJ and Thurber, 2003; Yang HF et al., 2009; Zheng Y et al., 2009; Fang LH et al., 2013; Long et al., 2019), analysis of the variation characteristics of the source spectrum with azimuth based on dense network observations (Tan Y and Helmberger, 2010; He XH and Ni SD, 2018; Xu YY and Wen LX, 2019), and geodetic methods based on InSAR data (Feng WP et al., 2013; Xu WB et al., 2015; Shan XJ et al., 2017; Jiang GY et al., 2018; Sun JB et al., 2018; Xu GY et al., 2019). Considering the significant magnitude of this earthquake, which caused noticeable deformation at the surface and was recorded by ascending and descending orbiting satellites, we use InSAR data to constrain the rupture fault responsible for this earthquake.

In this study, we first utilize the generalized Cut-and-Paste (gCAP) method (Zhu LP and Helmberger, 1996; Zhu LP and Helmberger, 2013; Sheng MH et al., 2020; Chu RS and Sheng MH, 2023) to initiate the source parameters of the Adassil earthquake through seismic waveform modeling. Following this, we utilize InSAR data tracking coseismic deformation to refine the earthquake source parameters by considering constraints derived from the seismic findings. The Multiple-peak Particle Swarm Optimization (MPSO) algorithm (Feng WP et al., 2013; Xu GY et al., 2019) is used to evaluate these crucial parameters. Additionally, in this study, we combine seismic and InSAR data to determine the source parameters. We explore different inversion strategies for seismic waveform and InSAR data, specifically focusing on determining the centroid depth during joint inversion. The results allow us to identify the seismogenic fault of the 2023 M_w 6.8 Adassil earthquake. Taking into account the occurrence of relatively deep earthquakes in the High Atlas and nearby volcanic activity, we infer the causative mechanism of this earthquake based on these tectonic activities.

2. Seismotectonic Setting

The High Atlas Mountain Range stretches 650 km along a west-southwest to east-northeast axis, comprising the Western, Central, and Eastern High Atlas sections. Notably, elevations in the Central High Atlas reach 3.5 to 4.0 km. This area exhibits geological diversity, with prominent volcanic activity and Mesozoic basalt structures emerging from ancient tectonic rifting. The Middle Atlas and the southern margin of the Western High Atlas have experienced significant alkaline basalt eruptions from the Paleogene to the Quaternary periods, reflecting a broader pattern of volcanism that was widespread throughout northwestern Africa and southern Spain from the Jurassic to the Neogene–Pleistocene epochs. Some studies (Mattei et al., 2014; Casalini et al., 2022) have documented that the most recent volcanic activities have synchronized with the orogenic evolution of the High Atlas, suggesting a lithosphere influenced by crustal compression (Laffitte, 1939; Ghandriche, 1991; Khomsi et al., 2004). During the more tranquil Oligocene–Miocene period, a considerable sedimentary sequence of siliciclastic and marine deposits formed in this region. A meticulous scrutiny of regional age data, as delineated in Figure 2b, demonstrates a northeastward migration of volcanic activity from the Middle Atlas. This shift signals that the topographical traits of the area might have a relatively younger geological provenance. Missenard et al. (2006) elucidated the timeline of tectonic and magmatic phases in Morocco, noting the inception of alkaline volcanism within the Atlas domain, which then spread southward to the Anti-Atlas, encompassing the Siroua and Sahro volcanoes and northward to the Rif, overtaking the previous calc-alkaline volcanism associated with subduction processes. According to Seber et al. (1996), the lithosphere of the High Atlas is relatively thin and shows significant thermal sensitivity, as supported by P-wave travel time data. These data are further supported by the receiver function analysis, suggesting an average lithospheric thickness of approximately 100 km, with variations ranging from 70 to 90 km, as proposed by the thermal and density models (Zeyen et al., 2005).

Global positioning system (GPS) datasets interpreted by Fadil et al. (2006) and Serpelloni et al. (2007) indicated a convergence rate of approximately 1–2 mm per annum in the High Atlas. Further geomorphological investigations (Lanari et al., 2020) indicated that tectonic activity plays a crucial role in shaping the High Atlas, with a noticeable decrement in transpressional forces observed toward the eastern extent of the range. Within the broader tectonic framework of Northwest Africa, the High Atlas is affected by a prominent right-lateral shear zone, primarily originating from oblique tectonic movements, as supported by the research of Soumaya et al. (2018) and Dewey et al. (1989). The complex transpressional tectonics of the High Atlas have become focal points in geological research. During the Cenozoic era, pre-existing Triassic–Jurassic structures in the High Atlas were reactivated, leading to strain partitioning and the development of oblique-slip faults within the range and thrust-related folds at its edges (Ellero et al., 2012; Lanari et al., 2020). Consequently, the tectonic architecture of the Central High Atlas is predominantly characterized by fold-and-thrust faulting mechanisms rather than by oblique-slip fault dynamics (Teixell et al., 2003; Calvín et al., 2018). This complex style of orogenic deformation significantly influences the variable magnitudes of crustal shortening observed across different transects. For example, the NNW–SSE-oriented sections exhibit shortening estimates ranging from approximately

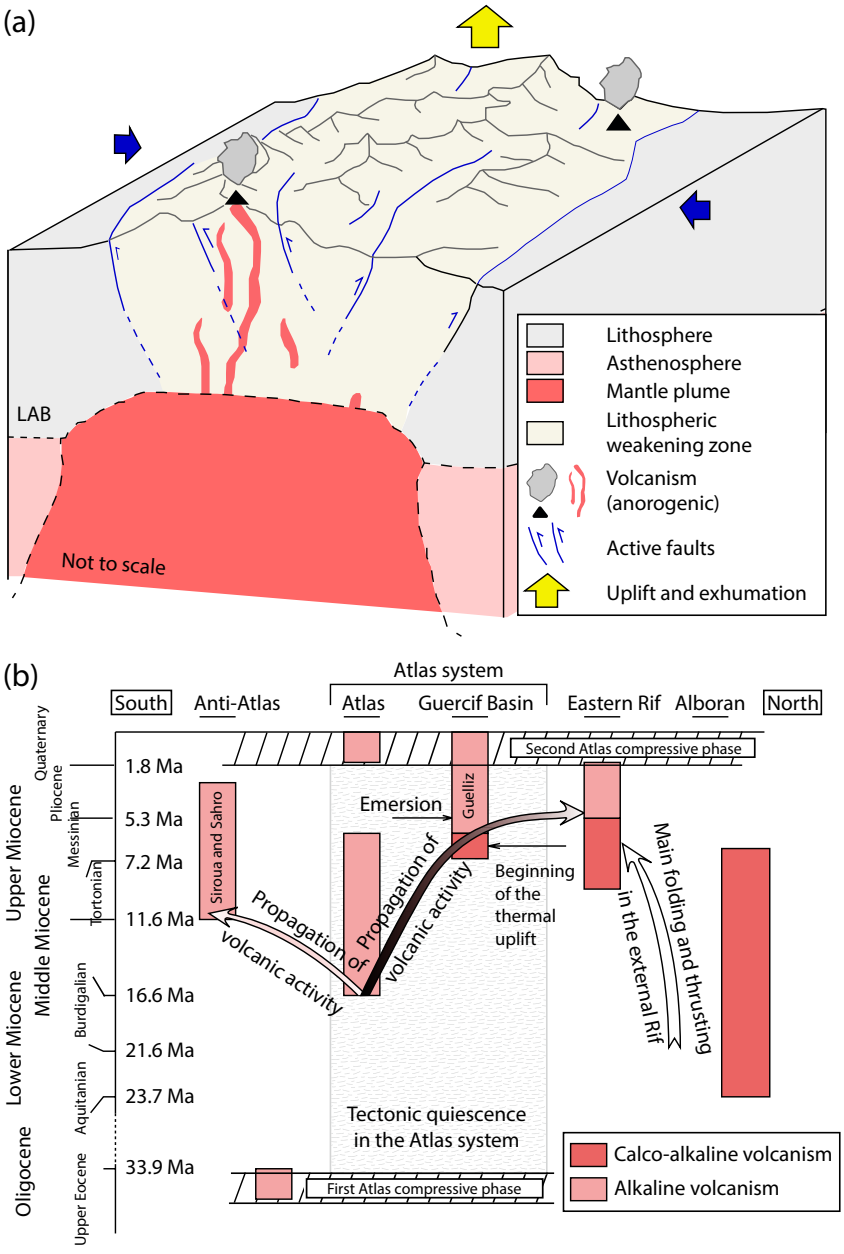

Figure 2. (a) Schematic evolution model of the High and Anti-Atlas for four different time intervals: Miocene–present post-mantle impingement (after Lanari et al., 2023). LAB, lithosphere–asthenosphere boundary. (b) Chronology of tectonic phases and magmatic activity in Morocco. This illustration depicts the sequence of tectonic phases and magmatic events in Morocco. Notably, alkaline volcanism initiated in the Atlas region, then spread both southward into the Anti-Atlas (manifesting in the Siroua and Sahro volcanoes) and northward into the Rif (where it replaced the calc-alkaline subduction-related volcanism). The well-documented uplift of the Guercif Basin, as highlighted by Krijgsman et al. (1999), aligns notably with the volcanic activity in the region. The ages of volcanic rocks are sourced from El Azzouzi et al. (1999) and De Beer et al. (2000) (after Missenard et al., 2006).

14 km, constituting 17%–20% shortening (Domènech et al., 2016; Fekkak et al., 2018). In the Western High Atlas, shortening is quantified at approximately 12–15 km, corresponding to 15%–21% (Teixell et al., 2003; Domènech et al., 2016). Conversely, in the axial zones of the Central High Atlas, deformation results in a more significant crustal shortening of 30–34 km, reflecting a 30% shortening (Beauchamp et al., 1999; Teixell et al., 2003). The 2023 Adassil earthquake sequence acts as an indicator of the tectonic activity within the High Atlas region. The convergence rates, thrust fault dynamics, and resultant morphological features provide valuable insights into the profound geodynamic forces sculpting the topography of the area.

Lanari et al. (2023) has revealed the significant role of geodynamic processes in shaping the unique topographical features of the High Atlas region (Figure 2a). The distinctive surface topography and magmatism observed in the Atlas region are attributed to mantle upwellings associated with the Canary Plume, lithospheric thinning, or a combination of both (Ramdani, 1998; Zeyen et al., 2005; Civiero et al., 2018). Lanari et al. (2023) further suggested

that lithospheric weakening may enhance crustal deformation even at slow convergence rates. Numerical simulations indicate that erosion caused by mantle upwelling could be a key factor in lithospheric thinning, potentially eliminating the necessity of delamination. Volcanic deposits within the rift strata suggest crustal thinning mechanisms similar to pure shear or related rift processes, along with thermal erosion from conductive heating. The presence of sharply defined lithospheric edges might indicate lithospheric removal via advective processes, such as delamination or vigorous drip-like convection (Carbonell et al., 2015). This understanding is further refined by recognizing the feedback between plume-induced lithospheric weakening and strain localization, a dynamic that is also observed in other convergent terrains where deep mantle processes trigger volcanism amid nappe stacking, similar to the cases of the Caucasus and Alborz belts. These findings shed light on the potential for mantle plume activity and associated volcanism to weaken the lithosphere beneath the Atlas, resulting in concentrated crustal shortening along pre-existing tectonic frameworks during plate convergence. This pattern could represent a widespread mechanism influencing continental plates across supercontinental cycles. The hypotheses supported by Lanari et al. (2023) suggested an increase in crustal deformation and exhumation during the middle to late Miocene, coinciding with the onset of volcanism, and indicate a likely deep mantle origin for the volcanism. That dynamic mantle upwelling plays a crucial role in maintaining the elevated topography of the Atlas.

3. Seismic Wave Inversion

We collected waveform data from the Incorporated Research Institutes for Seismology (IRIS) Data Management Center (DMC) to conduct focal mechanism inversion for this earthquake. Initially, we selected waveforms from teleseismic stations with epicentral distances ranging from 30° to 90°. The stations within this epicentral distance range exhibit a uniform distribution in terms of azimuth angles. Furthermore, these stations display relatively simple waveforms, which are suitable for accurately determining source parameters through waveform modeling. After performing preprocessing on the waveform data, including removing the mean value, linear trend, and instrument response, a manual inspection was conducted to eliminate data with a low signal-to-noise ratio (SNR). As a result, we obtained waveforms from 26 stations with high SNRs and well-distributed azimuth angles. The three-component velocity seismograms were then rotated to radial, tangential, and vertical (RTZ) components. At present, several techniques are available for inverting earthquake source parameters by using teleseismic data (Zhu LP and Hemlberger, 1996; Duputel et al., 2012; Ekström et al., 2012; Zang C et al., 2019; Jia Z et al., 2020). In this study, we used the gCAP approach, as described by Zang C et al. (2019), to perform inversion and determine the focal mechanism, moment magnitude, and centroid depth using teleseismic data. The algorithm uses vertical-component P waves and tangential-component SH waves to estimate source parameters. Additionally, independent time shifts were allowed for waveform segments to accommodate an inaccurate velocity model and imprecise event location. The time windows for P and SH waves were selected as 100 s and 150 s, respectively. The band-pass filters utilized for P and SH waves had frequency ranges of 0.02–0.1 Hz and 0.02–0.05 Hz, respectively. These frequency bands were specifically chosen to mitigate the influence of small-scale structures and reduce low-frequency noise across multiple stations. Green's functions were calculated using the propagation matrix method (Kikuchi and Kanamori, 1982; Chu RS et al., 2014), in conjunction with the CRUST1.0 velocity model (Laske et al., 2013).

Through a grid search, we obtained the optimal parameters. The inversion results are summarized in Table 1. The moment magnitude is M_w 6.86, and the source duration is 10 s. The two nodal planes were determined as 100°/25°/120° (NP1) and 247°/68°/76° (NP2), with an optimal centroid depth of 23 km (Figure 3). The analysis of waveform fitting revealed that a majority of waveforms exhibited a high degree of compatibility, with cross-correlation coefficients exceeding 90%. Nodal Plane 1 shows a notable deviation from the strike angles observed in Global CMT and USGS data (approximately 20°), whereas the disparities in other angular parameters do not exceed 12°. Moreover, the discrepancies in magnitude remain within a range of 0.1. These findings suggest a relatively high level of agreement among the results obtained by various institutes. The centroid depth determined by the gCAP method is approximately 23 km, which deviates significantly from the depth from Global CMT, approximately 5 km.

4. InSAR Inversion

Interferometric synthetic aperture radar has emerged as a transformative technology in Earth observation and geophysics in recent decades (Sun JB et al., 2011; Xu XH et al., 2020; Beldjoudi and Delouis 2022; Han BQ et al., 2022). It leverages the capabilities of radar imaging satellites to monitor ground deformations with exceptional precision and spatial coverage. One of the remarkable platforms that has enabled groundbreaking InSAR applications is the European Space Agency's Sentinel-1 satellite constellation. Comprising two polar-orbiting satellites, Sentinel-1A and Sentinel-1B, this mission has revolutionized our ability to monitor changes in the Earth's surface, making it an invaluable tool for a wide range

Table 1. Source parameters of the Adassil earthquake from different institutes.

Source	(Strike°/dip°/rake°)		Magnitude (M_w)	Centroid depth (km)
	NP1	NP2		
Global CMT	119/23/132	255/73/74	6.90	27.8
USGS (W-phase)	122/29/132	255/69/69	6.85	30.5
gCAP	100/25/120	247/68/76	6.87	23.0
InSAR	—	250/70/74	6.82	29.1

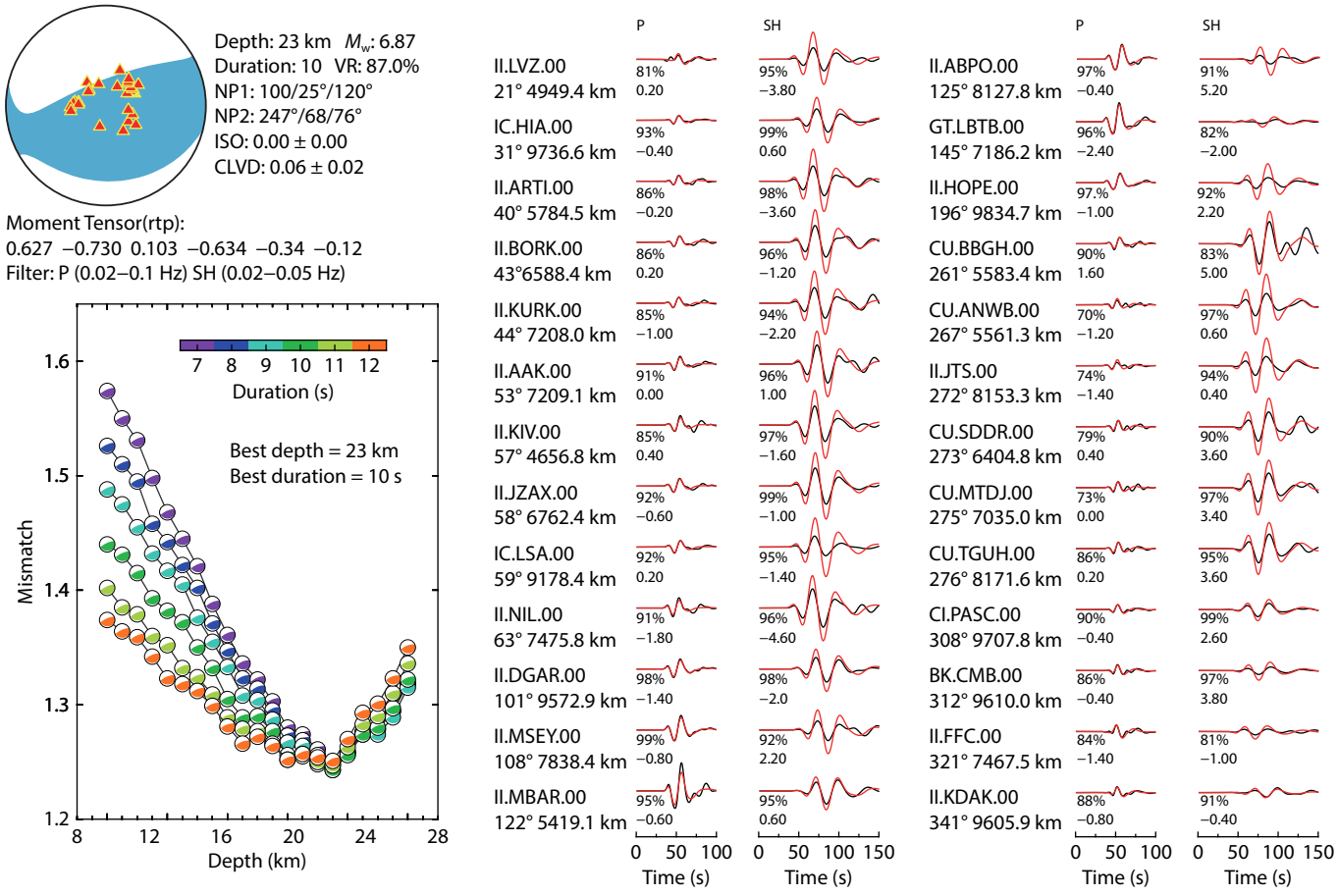

Figure 3. Point-source inversion results for the Adassil event. (a) The gCAP inversion results in the waveform residual versus source duration and centroid depth, with beach balls colored according to the source time functions. The numbers above and beneath the focal mechanism plot are the moment magnitude and centroid depth. The black and red traces indicate the observations and synthetics, respectively. The labels and numbers to the left side of the waveforms are the station code, azimuth, and epicenter distance. The upper and lower numbers close to the left of seismograms are cross-correlation coefficients (in percentages) and time shifts (in seconds), respectively.

of applications, including environmental monitoring, disaster management, and geophysical research. The frequent revisit times and all-weather imaging capabilities of Sentinel-1 make it suitable for monitoring dynamic and rapidly changing landscapes, including those affected by geological phenomena such as earthquakes and volcanic activity. In this context, Sentinel-1 has played a pivotal role in advancing our understanding of tectonic processes, seismic hazard assessment, and disaster response. Its ability to capture detailed deformation patterns before and after earthquakes has proven invaluable for studying earthquake source mechanisms and assessing associated risks. By providing high-quality InSAR data, Sentinel-1 empowers scientists and researchers to investigate the Earth's surface dynamics with unprecedented accuracy and timeliness.

Three image scenes covering the epicentral area of the Adassil earthquake were captured by the Sentinel-1 satellite. These images were captured during both descending and ascending orbits and were designated as T045A, T052D, and T154D. We adopted two coseismic line-of-sight displacements, in an ascending orbit (T045A) and a descending orbit (T154D), for earthquake source parameter inversion. Before implementing interferometry processing, the pre- and post-earthquake images underwent a registration process. To enhance the SNR of the image, a multilook ratio of 10:2 was applied in the range and azimuth directions. We utilized the GAMMA software for conducting differential interferometry processing to derive the coseismic deformation (Wang S et al., 2022). We utilized SRTM (Shuttle Radar Topography Mission) 30-m DEM (digital elevation model) data to mitigate the influence of terrain effects, as demonstrated by Farr et al. (2007). The interferogram was subjected to adaptive filtering by using the method proposed by Goldstein and Werner (1998). Subsequently, the interferogram was unwrapped by using the minimum cost flow method (Chen CW and Zebker, 2000). Finally, the geocoding process transformed the interferogram into the geographical coordinate system. We successfully derived the coseismic deformation field from the Adassil earthquake after converting the phase diagram into a deformation diagram.

We used a quadtree sampling method (Jónsson et al., 2002) to downsample the ascending and descending orbit images. After that, the ascending orbit image retained 570 deformation points, whereas the descending orbit image retained 626 points. During the inversion process, all data points were assigned equal weight. We used the MPSO algorithm (Feng WP et al., 2013; Xu GY et al., 2019) to search for nine parameters: fault top depth, fault bottom

depth, strike, dip, slip angle, slip amount, fault length, and epicenter location. The elastic half-space rectangular dislocation model (Okada, 1985) was adopted to calculate displacement based on source parameters. Initially, without considering the fault mechanism published by the seismic agency, we conducted a global search for the angle parameters, and other parameters had wide search ranges to avoid boundary effects. After 100 iterations, the results were distributed around the two fault plane solutions published by the seismic agency. The error on the north-dipping fault plane was 11.3 mm, whereas the error on the south-dipping fault plane was 11.4 mm. Despite the similar errors on both fault planes, the slip amount on the south-dipping fault plane was 5 m, reaching the upper limit set during the search. According to the relationship between the scale of most earthquake faults and slip amounts (Funning, 2005; Biggs et al., 2006; Gu WW et al., 2023), the north-dipping fault plane better conformed to this relationship. From our analysis of the interferograms (Figure 4) and downsampled deformation maps (Figure 5), we observed that the deformation is predominantly distributed on the northern side, mainly characterized by uplift. However, deformation is also present on the southern side, characterized by subsidence. The deformation gradient gradually decreases as we move northward, suggesting that the hanging wall of the fault is on the northern side, indicating a north-dipping fault. From the evidence above, we considered the fault plane with a strike of 250° (north-dipping fault plane) as the causative fault. Subsequently, we narrowed the search range for the parameters and performed another 100 iterations to obtain the optimal parameters, as shown in Table 1.

Using the optimal inversion results, we simulated the ascending and descending orbit deformation maps (Figure 3), as well as surface displacement maps (Figure 4), and obtained the corresponding residual maps. The forward model successfully reconstructed the deformation field. The residual diagram did not exhibit any discernible indications of deformation. The model residual was approximately 11.3 mm, indicating the reliability of our inversion results. The focal mechanism parameters derived from InSAR data exhibited a notable similarity to those from academic institutes using seismic data. The disparity between these results was limited to a maximum of 5°, whereas the discrepancy in magnitude remained within a range of 0.1. The centroid depth determined through InSAR was 29.1 km, which closely aligns with the results of the Global CMT and USGS analyses. However, it deviates from the results obtained through gCAP, which estimated a centroid depth of approximately 23.0 km.

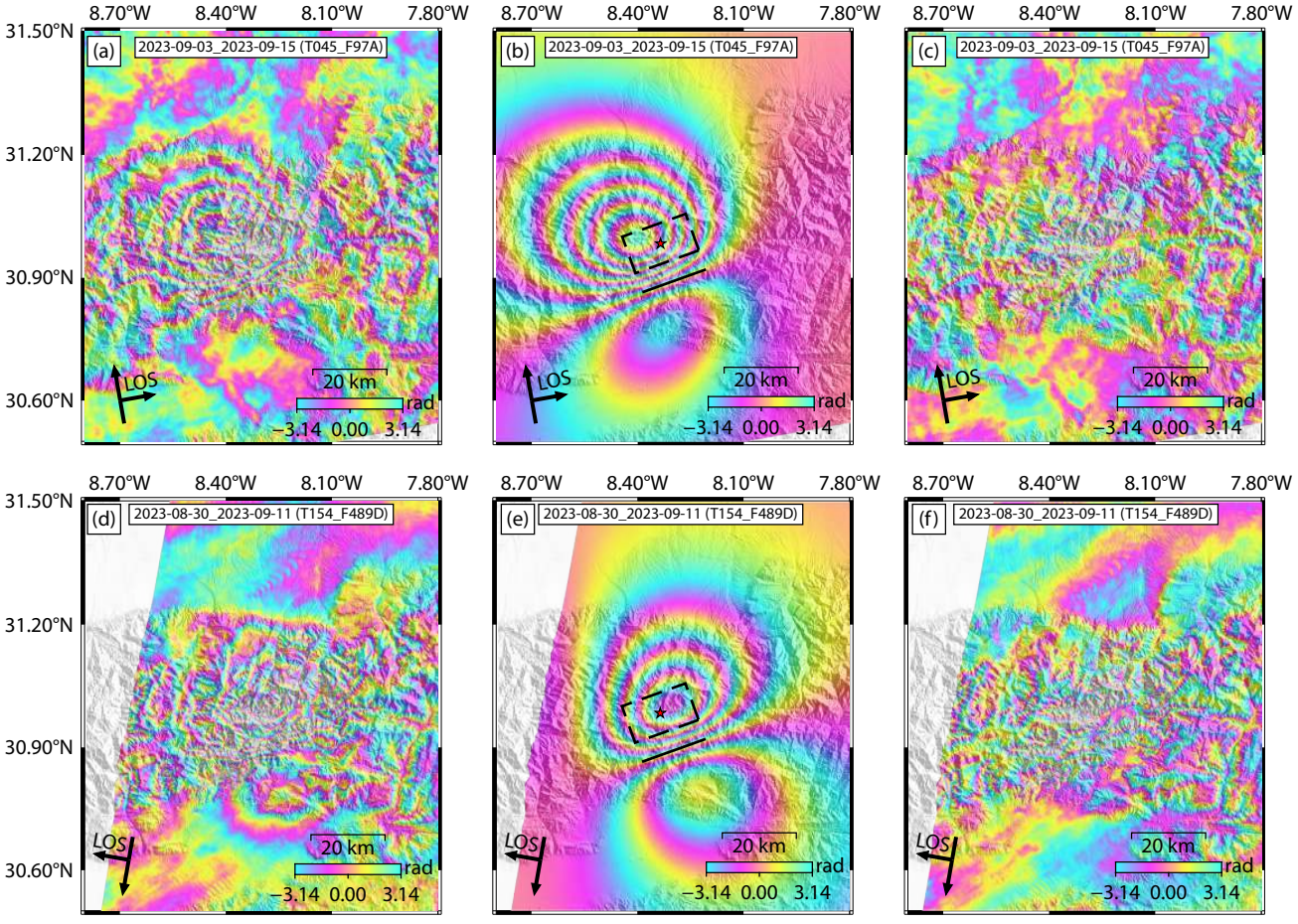

Figure 4. Coseismic displacement and model prediction of the 2023 M_w 6.8 Adassil earthquake are illustrated in wrapped Sentinel-1 data for both ascending (a) and descending (d) orbits. In the images, each fringe corresponds to half a wavelength of line-of-sight (LOS) displacement. The predicted InSAR data, displayed in panels (d) and (e), include the surface projection of the estimated fault plane denoted by a black dashed rectangle and the extrapolation of the fault plane to the surface represented by a black line. Residual phase information between the observed and predicted interferograms is depicted in panels (c) and (f), corresponding to the ascending (a) and descending (d) data sets.

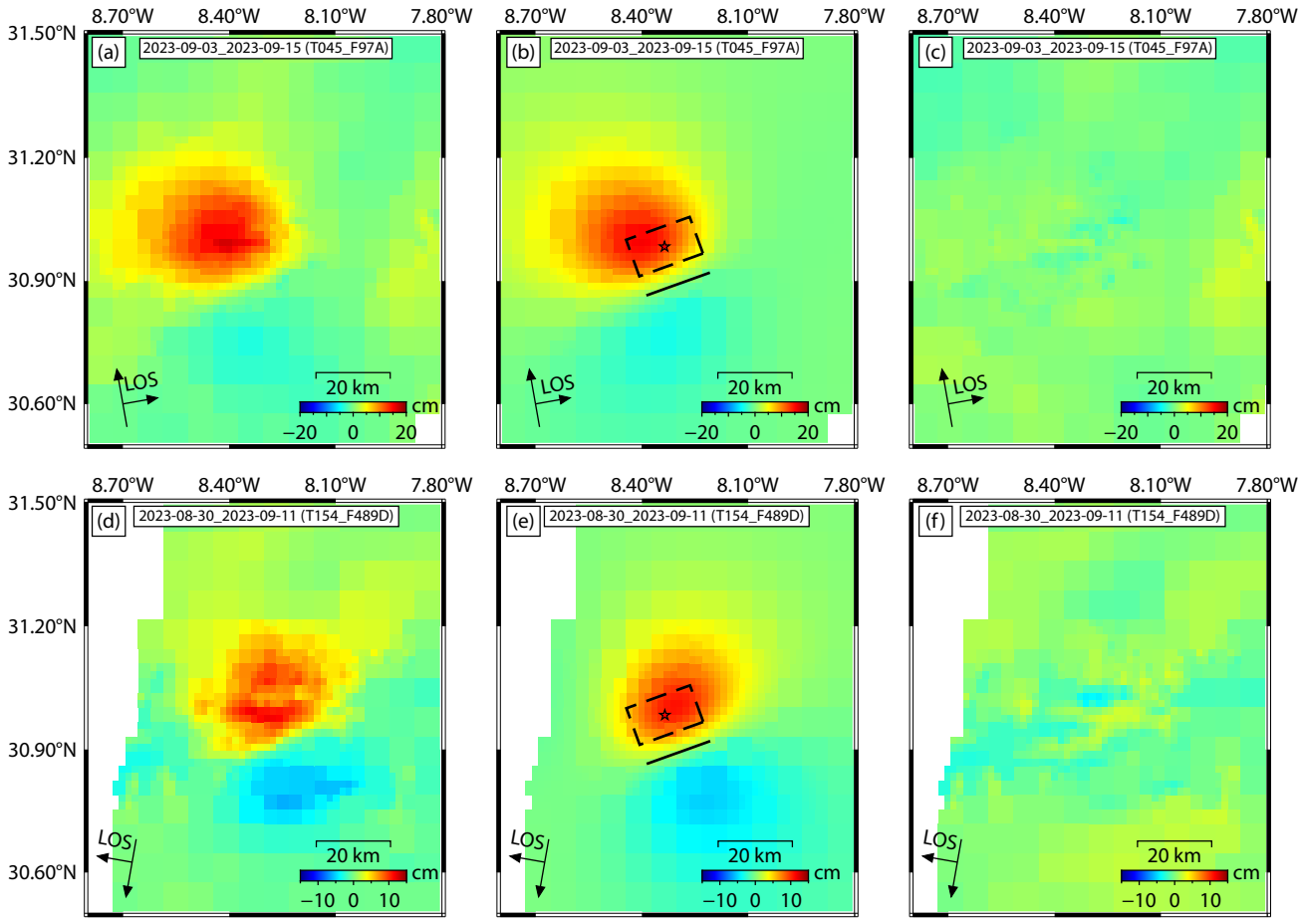

Figure 5. Downsampled InSAR and inversion results. Panels (a) and (d) in the first column show the observed interferograms. Panels (b) and (e) in the second column show the model prediction results. Panels (c) and (f) in the last column show the residuals between the observed interferograms and the model. Positive values indicate the ground moving toward the Setinel-1 satellite in the line-of-sight (LOS) direction. The surface projection of the estimated fault plane is denoted by a black dashed rectangle, and the extrapolation of the fault plane to the surface is represented by a black line.

5. Joint Inversion

We conducted separate inversions of the source parameters for the Adassil earthquake by using seismic and InSAR data, as discussed in the sections above. The strike/dip/rake parameters showed relatively consistent results, with differences within 5°, whereas significant variation was observed in the inferred depth of approximately 6 km. We utilized a joint inversion method to determine the source depth of the earthquake to address this discrepancy. In the individual inversion of InSAR data, we assumed a uniform sliding fault and searched for the upper and lower boundaries of the fault separately. We tested the sensitivity of InSAR data to these boundary depths (Figure 6a). First, while keeping the lower boundary fixed, we searched for different upper boundary depths in the range of 1–43 km, resulting in error curves for various depths (Figure 6a). Second, while keeping the upper boundary depth constant, we searched for the lower boundary depth within the range of 15–55 km, generating depth error curves as well (Figure 5a). The results indicated that InSAR data were more sensitive to the upper boundary of the fault and had a lower resolution for the lower boundary. This observation is consistent with that by Aki and Richards (2002), who suggested that surface displacements caused by earthquakes decrease inversely with the square of the depth, which explains the greater sensitivity of InSAR observations to the upper boundary of the fault. In the joint inversion, we fixed the upper boundary depth and searched for the error distribution corresponding to different depths by varying the lower boundary depth. Considering the unit differences of the seismic and InSAR data, we applied normalization to both types of data during the inversion process. The specific normalization process can be depicted as follows:

$$L = \frac{\text{norm}\,(d_i - c_i)}{\max\left[\text{norm}\,(d_i - c_i)\right]}, \tag{1}$$

where d_i represents the data that have been observed, c_i corresponds to the synthetic data, and i denotes the index that is associated with a specific set of inversions. The term norm is used to denote the L_2 norm, which quantifies the magnitude of a vector. On the other hand, the term max signifies the maximum value within a given set. After normalizing the errors, we assigned different weights to the two types of data. The sum of weighted errors is as follows:

$$\text{misfit} = \lambda_1 L_1 + \lambda_2 L_2, \tag{2}$$

where misfit denotes the error function used in joint inversion,

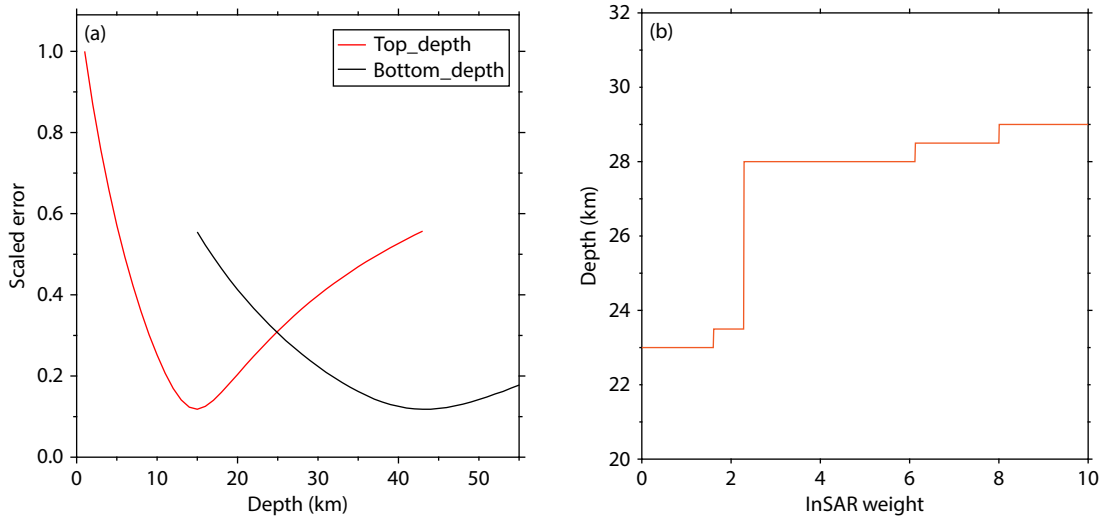

Figure 6. Variation of depth with the InSAR versus seismic data weight. (a) The variation of depth with scaled error. Top_depth represents different upper boundary depths versus scaled error with a fixed lower boundary. Bottom_depth represents different lower boundary depths versus scaled error with a fixed upper boundary. (b) The variation of depth with InSAR weight.

and the variables λ_1 and λ_2 are utilized as weighting factors to assign significance to seismic waveform and InSAR data, respectively. Additionally, L_1 and L_2 represent the squared errors of the normalized seismic waveform and InSAR data. We varied the InSAR weights from 0 to 10 with a step size of 0.01. By calculating the joint inversion error distribution for different weights (Figure 6b), we observed that as the InSAR weight increased, the centroid depth gradually rose from 23 to 29 km. The InSAR weight in the range of 3–6 yielded a stable centroid depth, indicating reliable results. The determined centroid depth of the Adassil earthquake was 28 km.

6. Discussion

The source parameters of the Adassil earthquake were determined by using seismic waves and InSAR data. The results indicate that the earthquake predominantly exhibited reverse motion, characterized by a steep dip angle with a strike direction of approximately 250°. The joint inversion analysis revealed that the centroid depth of the earthquake was approximately 28 km, which is beyond the typical depth range of 5–15 km for general tectonic earthquakes. When the depth of the seismic activity is less than 5 km, the structure in this region may exhibit a relatively low level of hardness, making it challenging to accumulate sufficient stress for the occurrence of moderate and strong earthquakes. On the other hand, when the depth of the earthquake exceeds 15 km, the rock undergoes changes in its physical properties resulting from temperature and pressure influences, leading to a transition from brittle deformation to plastic deformation. However, it is important to note that plastic deformation alone cannot accumulate the stress required for fault rupture.

In general, the temperature increases gradually as the depth increases. Nonetheless, it is worth noting that certain regions exhibit comparatively lower temperatures within the crust, thereby facilitating the occurrence of moderately intense seismic activity in the lower crust. Notable examples include the M_w 7.7 Bhuj earthquake in 2001 (Mandal et al., 2004), the M_w 5.2 Chifeng earthquake in 2009 (Wei SJ et al., 2009), and the M_w 6.6 Hokkaido earthquake in 2018 (Zang C et al., 2019). Although differences exist in the mechanisms of these earthquakes, such as the predominantly strike-slip nature of the Chifeng earthquake and the predominantly thrust nature of the Bhuj and Hokkaido earthquakes, the hypocenters of these earthquakes are all relatively deep, with the epicenters of both the Chifeng earthquake and the Hokkaido earthquake situated at relatively lower temperatures. Gosset (2004) found that the crustal thickness in the source region of the Adassil earthquake is approximately 30–35 km. On the basis of the centroid depth of this earthquake, it can be inferred that the lower crustal rocks in the High Atlas area have relatively low temperatures. This lower temperature facilitates the accumulation of significant stress, leading to subsequent rupture and the occurrence of earthquakes.

According to the teleseismic waveform inversion results, two distinct nodal planes of the Adassil earthquake are derived. One exhibits a low dip angle, whereas the other demonstrates a high dip angle. In both cases, the predominant mechanism is a reverse fault, accompanied by a minor contribution of strike-slip motion. The seismogenic fault of this earthquake was identified as a high-dip reverse fault based on InSAR inversion results. The results of various institutes align with the seismic wave inversion results presented in this article, supporting the reliability of the approximately 70° dip angle obtained in this study. In general, high-dip reverse faults are difficult to rupture (Sibson, 1985). The fulfillment of the Mohr–Coulomb rupture criterion for the activation of high-dip reverse faults can occur in the presence of high-pressure fluid on the fault. The 2018 Hokkaido earthquake was classified as a high-dip reverse event (Zang C et al., 2019) that occurred within the lower crust. Zang C et al. (2019) demonstrated the coexistence of a cold fore-arc and a hot volcanic arc nearby. The presence of a cold fore-arc region creates favorable stress conditions for the occurrence of earthquakes.

In contrast, the interaction between the hot volcanic arc and the

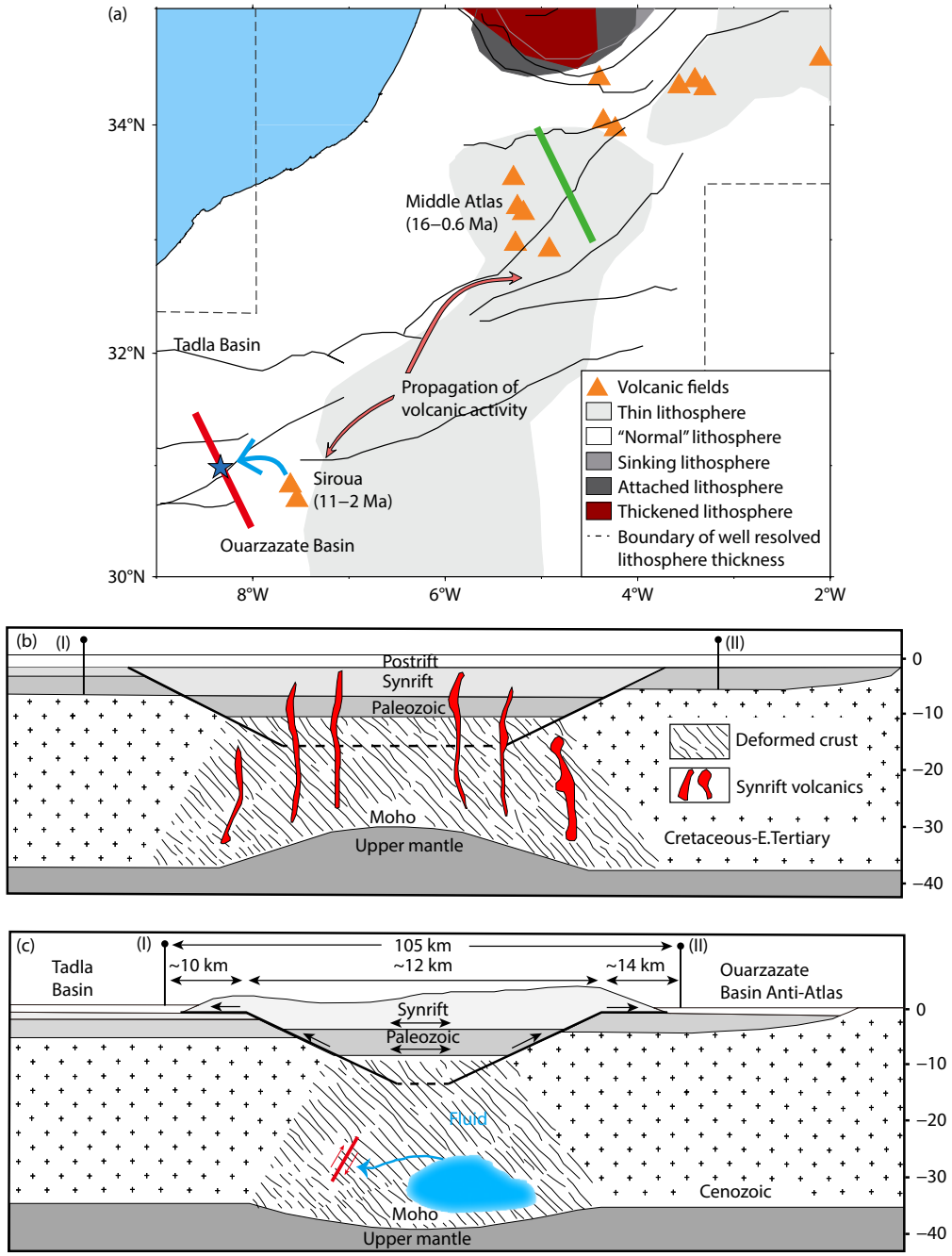

Figure 7. (a) Composite plot illustrating the notable impedance locations in the velocity and structural models. Detailed model characteristics can be found in other references (Bezada et al., 2013; Palomeras et al., 2014; Thurner et al., 2014). The image provided depicts a cartographic representation of diverse lithospheric characteristics, notably highlighting the shallow rheological properties of the boundary between the lithosphere and asthenosphere (commonly referred to as the LAB). Furthermore, it serves to indicate the geographic positions of surface volcanic fields (after Carbonell et al., 2015). (b, c) Schematic cross-sections that depict the tectonic evolution of the Atlas Rift system. The final uplift and inversion phase demonstrates the process of uplifting and inverting the Atlas Rift system, ultimately leading to the creation of the contemporary Atlas Mountains. The inversion observed can be attributed to the convergence of the African and Iberian plates, which occurred during the Tertiary period, specifically within the Miocene to Oligocene epochs. The process entailed the application of forces in opposing directions along the boundaries of the rift, occurring at depths within the Earth's crust that are relatively shallow. These forces were exerted over relatively limited distances, estimated to be between 10 and 14 km. Significantly, a notable reduction in compression was observed within the interior of the mountain range, indicating that most of the contraction occurred at depths within the middle to lower crust. The postrift phase is characterized by the subsidence from the Late Jurassic to Tertiary periods. Panel (b) represents the structure of the green line in panel (a). Panel (c) represents the structure of the red line in panel (a). The red line in panel (c) indicates the seismogenic fault of the Adassil earthquake (after Beauchamp et al., 1999).

cold fore-arc can generate an environment abundant in fluids. Contemporary research indicates that the High Atlas region experiences thermal anomalies and crustal shortening, resulting in an elevation of approximately 4 km. Figure 7a demonstrates that volcanic activity originates from the High Atlas Mountains and subsequently extends northward, encompassing the Middle Atlas region, and southward, specifically affecting the Anti-Atlas area, which includes the Siroua and Sahro volcanoes. Roughly 10 million years ago, the region experienced a significant occurrence of volcanic activity, which appears to correlate with the thinning of the lithosphere in this area. Over time, these rocks underwent a gradual cooling process, resulting in a geological setting rich in fluids within the crust. The temperature of these rocks decreased to a relatively low level, and the M_w 6.8 Adassil earthquake occurred under these circumstances.

Nevertheless, it is worth noting that volcanic activity in the High Atlas region lasts for a relatively longer duration, causing the rocks in the Siroua area to undergo a slower cooling process and resulting in lower temperatures. The Siroua area, where the earthquake occurred, differs from the High Atlas region in its geological characteristics, specifically with a cold, fluid-rich environment. The geological composition of the region is highly complex, requiring careful consideration of the associated seismic hazard. Additionally, the temporal patterns of volcanic activity in the Middle Atlas region are similar to those observed in the Siroua region. Moreover, because of the infrequent seismic events in this region and its considerable distance from the plate boundary, further research is needed in this area. Therefore, additional studies are required to support the findings presented in this article.

7. Conclusions

We present a study on the kinematic source parameters of the 2023 Adassil earthquake by using seismic waves and InSAR data. The results of point-source inversion revealed that the event is a reverse earthquake. The causative fault exhibits a high dip angle and a strike direction of approximately 250° with a centroid depth of approximately 28 km. This unusual depth, exceeding the typical seismogenic thickness, suggests that lower crustal rocks in the High Atlas region may have cooler temperatures, which can facilitate stress accumulation and seismic rupture. This finding is consistent with observations in similar tectonic settings, where fluid-rich environments and thermal anomalies within the crust promote the occurrence of earthquakes. The geological complexity of the Siroua area and its cold and fluid-rich composition demands an enhanced understanding of the seismic hazard it poses. Despite the sparse seismic activity and its significant distance from plate boundaries, further research is crucial to deepen our understanding of the seismotectonic behavior in this region. Additionally, future research should focus on the propagation of volcanic activity toward the Middle Atlas. Our study contributes to understanding deep crustal earthquakes, and we emphasize the importance of continuous surveillance and further investigation, particularly in regions with atypical earthquakes.

Acknowledgments

The seismic waveform data used in this paper were acquired from the IRIS DMC (http://ds.iris.edu). The Sentinel-1 image used in this article was provided by the European Space Agency. The Seismic Analysis Code was used for data processing, and Generic Mapping Tools were used for figure plotting. We thank the reviewers for their valuable comments and suggestions. This work was supported by the National Natural Science Foundation of China (Grant Nos. 42030311, and 42325401) and the Science and Technology Innovation Talent Program of Hubei Province (Grant No. 2022EJD015).

References

Aki, K., and Richards, P. G. (2002). *Quantitative Seismology* (2nd ed., p. 34). Sausalito, California: University Science Books.

Beauchamp, W., Allmendinger, R. W., Barazangi, M., Demnati, A., El Alji, M., and Dahmani, M. (1999). Inversion tectonics and the evolution of the High Atlas Mountains, Morocco, based on a geological-geophysical transect. *Tectonics*, *18*(2), 163–184. https://doi.org/10.1029/1998TC900015

Beldjoudi, H., and Delouis, B. (2022). Reassessing the rupture process of the 2003 Boumerdes–Zemmouri earthquake (M_w 6.8, northern Algeria) using teleseismic, strong motion, InSAR, GPS, and coastal uplift data. *Mediterr. Geosci. Rev.*, *4*(4), 471–494. https://doi.org/10.1007/s42990-022-00090-z

Bezada, M. J., Humphreys, E. D., Toomey, D. R., Harnafi, M., Dávila, J. M., and Gallart, J. (2013). Evidence for slab rollback in westernmost Mediterranean from improved upper mantle imaging. *Earth Planet. Sci. Lett.*, *368*, 51–60. https://doi.org/10.1016/j.epsl.2013.02.024

Biggs, J., Bergman, E., Emmerson, B., Funning, G. J., Jackson, J., Parsons, B., and Wright, T. J. (2006). Fault identification for buried strike-slip earthquakes using InSAR: The 1994 and 2004 Al Hoceima, Morocco earthquakes. *Geophys. J. Int.*, *166*(3), 1347–1362. https://doi.org/10.1111/j.1365-246x.2006.03071.x

Calvín, P., Casas-Sainz, A. M., Villalaín, J. J., and Moussaid, B. (2018). Extensional vs. compressional deformation in the Central High Atlas salt province: A paleomagnetic approach. *Tectonophysics*, *734*, 130–147. https://doi.org/10.1016/j.tecto.2018.04.007

Carbonell, R., Díaz, J., Harnafi, M., El Hassani, A., Ayarza, P., Gil, A., Gallart, J., Torné, M., Mancilla, F., Palomeras, I., and Levander, A. (2015). The crust beneath Morocco: From the surface topography to the upper mantle a 700 km long seismic section across Morocco. *Bulletin d'Information de l' Académie Hassan II des Sciences et Techniques*, 1, 31–46. http://hdl.handle.net/10261/152721

Casalini, M., Tommasini, S., Guarnieri, L., Avanzinelli, R., Lanari, R., Mattei, M., and Conticelli, S. (2022). Subduction-related lamproitic signature in intraplate-like volcanic rocks: The case study of the Tallante alkali basalts, Betic Chain, South-eastern Spain. *Ital. J. Geosci.*, *141*(1), 144–159. https://doi.org/10.3301/ijg.2022.06

Chen, C. W., and Zebker, H. A. (2000). Network approaches to two-dimensional phase unwrapping: Intractability and two new algorithms. *J. Opt. Soc. Am. A*, *17*(3), 401–414. https://doi.org/10.1364/josaa.17.000401

Cherkaoui, T. E., and El Hassani, A. (2012). Seismicity and seismic hazard in Morocco 1901–2010. *Bulletin de l'Institut Scientifique, Rabat, section Sciences de la Terre*, (34), 45–55. http://www.israbat.ac.ma/wp-content/uploads/2015/01/05-Cherkaoui_BIS_ST34_45.pdf

Chu, R. S., Ni, S. D., Pitarka, A., and Helmberger, D. V. (2014). Inversion of source parameters for moderate earthquakes using short-period teleseismic *P* waves. *Pure Appl. Geophys.*, *171*(7), 1329–1341. https://doi.org/10.1007/s00024-013-0719-1

Chu, R. S., and Sheng, M. H. (2023). Stress features inferred from induced earthquakes in the Weiyuan shale gas block in southwestern China. *J. Geophys. Res.: Solid Earth*, *128*(2), e2022JB025344. https://doi.org/10.1029/2022jb025344

Civiero, C., Strak, V., Custódio, S., Silveira, G., Rawlinson, N., Arroucau, P., and Corela, C. (2018). A common deep source for upper-mantle upwellings below the Ibero-western Maghreb region from teleseismic *P*-wave travel-time tomography. *Earth Planet. Sci. Lett.*, *499*, 157–172. https://doi.org/10.1016/j.epsl.2018.07.024

De Beer, C. H., Chevallier, L. P., De Kock, G. S., Gresse, P. G., and Thomas, R. J.

(2000). Carte géologique du Maroc au 1/50 000, feuille Sirwa. Notice explicative. Notes et Mem. Serv. Geol. Maroc 395bis, 86 pp.

Dewey, J. F., Helman, M. L., Knott, S. D., Turco, E., and Hutton, D. H. W. (1989). Kinematics of the western Mediterranean. *Geol. Soc., Lond., Spec. Publ., 45*(1), 265–283. https://doi.org/10.1144/gsl.sp.1989.045.01.15.

Domènech, M., Teixell, A., and Stockli, D. F. (2016). Magnitude of rift-related burial and orogenic contraction in the Marrakech High Atlas revealed by zircon (U-Th)/He thermochronology and thermal modeling. *Tectonics*, *35*(11), 2609–2635. https://doi.org/10.1002/2016tc004283

Duputel, Z., Rivera, L., Kanamori, H., and Hayes, G. (2012). W phase source inversion for moderate to large earthquakes (1990–2010). *Geophys. J. Int.*, *189*(2), 1125–1147. https://doi.org/10.1111/j.1365-246X.2012.05419.x

Ekström, G., Nettles, M., and Dziewoński, A. M. (2012). The Global CMT Project 2004–2010: Centroid-moment tensors for 13,017 earthquakes. *Phys. Earth Planet. Inter., 200–201*, 1–9. https://doi/org/10.1016/j.pepi.2012.04.002

El Azzouzi, M., Bernard-Griffiths, J., Bellon, H., Maury, R. C., Pique, A., Fourcade, S., Cotten, J., and Hernandez, J. (1999). Evolution of the sources of Moroccan volcanism during the Neogene. *Earth Planet. Sci., 329*, 95–102. https://www.researchgate.net/publication/263420782_Evolution_of_the_sources_of_Moroccan_volcanism_during_the_Neogene

Ellero, A., Ottria, G., Malusà, M. G., and Ouanaimi, H. (2012). Structural geological analysis of the high Atlas (Morocco): Evidences of a transpressional fold-thrust belt. In E. Sharkov (Ed.), *Tectonics—Recent Advances*. London: InTechOpen, 229-258. https://doi.org/10.5772/50071

Fadil, A., Vernant, P., McClusky, S., Reilinger, R., Gomez, F., Sari, D. B., Mourabit, T., Feigl, K., and Barazangi, M. (2006). Active tectonics of the western Mediterranean: Geodetic evidence for rollback of a delaminated subcontinental lithospheric slab beneath the Rif Mountains, Morocco. *Geology*, *34*(7), 529–532. https://doi.org/10.1130/G22291.1

Fang, L. H., Wu, J. P., Wang, W. L., Lü, Z. Y., Wang, C. Z., Yang, T., and Cai, Y. (2013). Relocation of the mainshock and aftershock sequences of M_S 7.0 Sichuan Lushan earthquake. *Chin. Sci. Bull.*, *58*(28-29), 3451–3459. https://doi.org/10.1007/s11434-013-6000-2

Farr, T. G., Rosen, P. A., Caro, E., Crippen, R., Duren, R., Hensley, S., Kobrick, M., Paller, M., Rodriguez, E., … Alsdorf, D. (2007). The shuttle radar topography mission. *Rev. Geophys., 45*(2), RG2004. https://doi.org/10.1029/2005rg000183

Fekkak, A., Ouanaimi, H., Michard, A., Soulaimani, A., Ettachfini, E. M., Berrada, I., El Arabi, H., Lagnaoui, A., and Saddiqi, O. (2018). Thick-skinned tectonics in a Late Cretaceous–Neogene intracontinental belt (High Atlas Mountains, Morocco): The flat-ramp fault control on basement shortening and cover folding. *J. Afr. Earth Sci., 140*, 169–188. https://doi.org/10.1016/j.jafrearsci.2018.01.008

Feng, W. P., Li, Z. H., Elliott, J. R., Fukushima, Y., Hoey, T., Singleton, A., Cook, R., and Xu, Z. H. (2013). The 2011 M_W 6.8 Burma earthquake: Fault constraints provided by multiple SAR techniques. *Geophys. J. Int.*, *195*(1), 650–660. https://doi.org/10.1093/gji/ggt254

Funning, J. G. (2005). Source parameters of large shallow earthquakes in the Alpine-Himalayan Belt from InSAR and waveform modelling [Ph. D. thesis]. Oxford: University of Oxford.

Ghandriche, H. (1991). Modes of the superposition of Alpine age folding and thrust structures in the Aurès (Algeria) [Ph. D. thesis]. Orsay, France: University of Paris Sud. (In French)

Goldstein, R. M., and Werner, C. L. (1998). Radar interferogram filtering for geophysical applications. *Geophys. Res. Lett.*, *25*(21), 4035–4038. https://doi.org/10.1029/1998gl900033

Gosset, C. (2004). The Origin of the Topography of the Anti Atlas (Morocco: Constraints Provided by Geology and Quantitative Geomorphology) (in French) [Master's thesis]. The University of Paris-6.

Gu, W. W., Ni, S. D., Wang, S. F., Zhang, B. L., Lei, X. L., Chu, R. S., Guo, A. Z., Shen, Q., Wang, H. S., ... Chong, J. J. (2023). Causative fault and seismogenic mechanism of the 2010 Suining *M*5.0 earthquake from joint modeling of seismic and InSAR data. *Sci. China Earth Sci.*, *66*(8), 1825–1838. https://doi.org/10.1007/s11430-022-1104-5

Han, B. Q., Yang, C. S., Li, Z. H., Yu, C., Zhao, C. Y., and Zhang, Q. (2022). Coseismic and postseismic deformation of the 2016 M_W6.0 Petermann ranges earthquake from satellite radar observations. *Adv. Space Res.*, *69*(1), 376–385. https://doi.org/10.1016/j.asr.2021.10.043

He, X., and Ni, S. (2018). Resolving horizontal rupture directivity of moderate crustal earthquake in sparse network with ambient noise location. *J. Geophys. Res.: Solid Earth*, *123*(1), 533–552. https://doi.org/10.1002/2017jb014735

Huang, M. H., Tung, H., Fielding, E. J., Huang, H. H., Liang, C. R., Huang, C. N., and Hu, J. C. (2016). Multiple fault slip triggered above the 2016 M_w 6.4 Meinong earthquake in Taiwan. *Geophys. Res. Lett.*, *43*(14), 7459–7467. https://doi.org/10.1002/2016GL069351

Jia, Z., Shen, Z. C., Zhan, Z. W., Li, C. Y., Peng, Z. G., and Gurnis, M. (2020). The 2018 Fiji M_w 8.2 and 7.9 deep earthquakes: One doublet in two slabs. *Earth Planet. Sci. Lett., 531*, 115997. https://doi.org/10.1016/j.epsl.2019.115997

Jiang, G. Y., Wen, Y. M., Li, K., Fang, L. H., Xu, C. J., Zhang, Y., and Xu, X. W. (2018). A NE-trending oblique-slip fault responsible for the 2016 Zaduo earthquake (Qinghai, China) revealed by InSAR data. *Pure Appl. Geophys., 175*(12), 4275–4288. https://doi.org/10.1007/s00024-018-1948-0

Jónsson, S., Zebker, H., Segall, P., Amelung, F. (2002). Fault Slip Distribution of the 1999 Mw 7.1 Hector Mine, California, Earthquake, Estimated from Satellite Radar and GPS Measurements. *Bull. Seismol. Soc. Am., 92*(4), 1377–1389. https://doi.org/10.1785/0120000922

Khomsi, S., Bédir, M., Zouari, H., and Ghazi Ben Jemia, M. (2004). Identification and Analysis of a Submerged Atlasic Structure at the Front of the Tunisian Alpine Chain. *C. R. Geosci. (in French), 336*(14), 1293–1300. https://doi.org/10.1016/j.crte.2004.05.003

Kikuchi, M., and Kanamori, H. (1982). Inversion of complex body waves. *Bull. Seismol. Soc. Am., 72*(2), 491–506. https://doi.org/10.1785/BSSA0720020491

Krijgsman, W., Langereis, C. G., Zachariasse, W. J., Boccaletti, M., Moratti, G., Gelati, R., Iaccarino, S., Papani, G., and Villa, G. (1999). Late Neogene evolution of the Taza–Guercif Basin (Rifian Corridor, Morocco) and implications for the Messinian salinity crisis. *Mar. Geol., 153*(1-4), 147–160. https://doi.org/10.1016/S0025-3227(98)00084-X

Laffitte, R. (1939). Geological Study of the Aurès (Algeria) (in French) [Ph. D. thesis]. Paris: Faculty of Sciences of the University of Paris.

Lanari, R., Fellin, M. G., Faccenna, C., Balestrieri, M. L., Pazzaglia, F. J., Youbi, N., and Maden, C. (2020). Exhumation and surface evolution of the Western High Atlas and surrounding regions as constrained by low-temperature thermochronology. *Tectonics*, *39*(3), e2019TC005562. https://doi.org/10.1029/2019tc005562

Lanari, R., Faccenna, C., Natali, C., Uluocak, E. Ş., Fellin, M. G., Becker, T. W., Göğüş, O. H., Youbi, N., Clementucci, R., and Conticelli, S. (2023). The Atlas of Morocco: A plume-assisted orogeny. *Geochem. Geophys. Geosyst., 24*(6), e2022GC010843. https://doi.org/10.1029/2022GC010843

Laske, G., Masters, G., Ma, Z. T., and Pasyanos, M. (2013). Update on CRUST1.0: A 1-degree global model of Earth's crust. In *EGU General Assembly Conference Abstracts*. Vienna, Austria: EGU.

Levandowski, W. (2023). Fault-slip potential near the deadly 8 September 2023 M_w 6.8 Al Haouz, Morocco, Earthquake. *The Seismic Record*, *3*(4), 367–375. https://doi.org/10.1785/0320230037

Long, F., Yi, G. X., Wang, S. W., Qi, Y. P., and Zhao, M. (2019). Geometry and tectonic deformation of the seismogenic structure for the 8 August 2017 MS 7.0 Jiuzhaigou earthquake sequence, northern Sichuan, China. *Earth Planet. Phys., 3*(3), 253–267. https://doi.org/10.26464/epp2019027

Maggi, A., Jackson, J. A., McKenzie, D., and Priestley, K. (2000). Earthquake focal depths, effective elastic thickness, and the strength of the continental lithosphere. *Geology*, *28*(6), 495–498. https://doi.org/10.1130/0091-7613(2000)28<495:efdeet>2.0.co;2

Mandal, P., Rastogi, B. K., Satyanaraya, H. V. S., Kousalya, M., Vijayraghavan, R., Satyamurty, C., Raju, I. P., Sarma, A. N. S., and Kumar, N. (2004). Characterization of the causative fault system for the 2001 Bhuj Earthquake of M_w 7.7. *Tectonophysics, 378*(1–2), 105–121. https://doi.org/10.1016/j.tecto.2003.08.026.

Mattei, M., Riggs, N. R., Giordano, G., Guarnieri, L., Cifelli, F., Soriano, C. C., Jicha, B., Jasim, A., Marchionni, S., ... Conticelli, S. (2014). Geochronology, geochemistry and geodynamics of the Cabo de Gata volcanic zone, Southeastern Spain. *Ital. J. Geosci., 133*(3), 341–361. https://doi.org/10.3301/ijg.2014.44

Missenard, Y., Zeyen, H., de Lamotte, D. F., Leturmy, P., Petit, C., Sébrier, M., and Saddiqi, O. (2006). Crustal versus asthenospheric origin of relief of the Atlas Mountains of Morocco. *J. Geophys. Res.: Solid Earth*, *111*(B3), B03401. https://

doi.org/10.1029/2005jb003708

Okada, Y. (1985). Surface deformation due to shear and tensile faults in a half-space. *Bull. Seismol. Soc. Am.*, *75*(4), 1135–1154. https://doi.org/10.1785/bssa0750041135

Palomeras, I., Thurner, S., Levander, A., Liu, K., Villasenor, A., Carbonell, R., and Harnafi, M. (2014). Finite-frequency Rayleigh wave tomography of the western Mediterranean: Mapping its lithospheric structure. *Geochem. Geophys. Geosyst.*, *15*(1), 140–160. https://doi.org/10.1002/2013GC004861

Peláez, J. A. (2023). Deadly Morocco quake resulted from Africa's ongoing collision with Europe. *Temblor*, http://doi.org/10.32858/temblor.321

Ramdani, F. (1998). Geodynamic implications of intermediate-depth earthquakes and volcanism in the intraplate Atlas Mountains (Morocco). *Phys. Earth Planet. Inter.*, *108*(3), 245–260. https://doi.org/10.1016/S0031-9201(98)00106-X

Seber, D., Barazangi, M., Tadili, B. A., Ramdani, M., Ibenbrahim, A., and Ben Sari, D. (1996). Three-dimensional upper mantle structure beneath the intraplate Atlas and interplate Rif mountains of Morocco. *J. Geophys. Res.: Solid Earth*, *101*(B2), 3125–3138. https://doi.org/10.1029/95JB03112

Serpelloni, E., Vannucci, G., Pondrelli, S., Argnani, A., Casula, G., Anzidei, M., Baldi, P., and Gasperini, P. (2007). Kinematics of the Western Africa-Eurasia plate boundary from focal mechanisms and GPS data. *Geophys. J. Int.*, *169*(3), 1180–1200. https://doi.org/10.1111/j.1365-246X.2007.03367.x

Shan, X. J., Qu, C. Y., Gong, W. Y., Zhao, D. Z., Zhang, Y. F., Zhang, G. H., Song, X. G., Liu, Y. H., and Zhang, G. F. (2017). Coseismic deformation field of the Jiuzhaigou M_S7.0 earthquake from Sentinel-1A InSAR data and fault slip inversion. *Chinese J. Geophys. (in Chinese)*, *60*(12), 4527–4536. https://doi.org/10.6038/cjg20171201

Sheng, M. H., Chu, R. S., Ni, S. D., Wang, Y., Jiang, L. M., and Yang, H. F. (2020). Source parameters of three moderate size earthquakes in Weiyuan, China, and their relations to shale gas hydraulic fracturing. *J. Geophys. Res.: Solid Earth*, *125*(10), e2020JB019932. https://doi.org/10.1029/2020jb019932

Sibson, R. H. (1985). A note on fault reactivation. *J. Struct. Geol.*, *7*(6), 751–754. https://doi.org/10.1016/0191-8141(85)90150-6

Soumaya, A., Ben Ayed, N., Rajabi, M., Meghraoui, M., Delvaux, D., Kadri, A., Ziegler, M., Maouche, S., and Braham, A. (2018). Active faulting geometry and stress pattern near complex strike-slip systems along the Maghreb region: Constraints on active convergence in the Western Mediterranean. *Tectonics*, *37*(9), 3148–3173. https://doi.org/10.1029/2018TC004983

Sun, J. B., Johnson, K. M., Cao, Z. Q., Shen, Z. K., Bürgmann, R., and Xu, X. W. (2011). Mechanical constraints on inversion of coseismic geodetic data for fault slip and geometry: Example from InSAR observation of the 6 October 2008 M_W6.3 Dangxiong-Yangyi (Tibet) earthquake. *J. Geophys. Res.: Solid Earth*, *116*(B1), B01406. https://doi.org/10.1029/2010JB007849

Sun, J. B., Yue, H., Shen, Z. K., Fang, L. H., Zhan, Y., and Sun, X. Y. (2018). The 2017 Jiuzhaigou earthquake: A complicated event occurred in a young fault system. *Geophys. Res. Lett.*, *45*(5), 2230–2240. https://doi.org/10.1002/2017GL076421

Tan, Y., and Helmberger, D. (2010). Rupture directivity characteristics of the 2003 Big Bear sequence. *Bull. Seismol. Soc. Am.*, *100*(3), 1089–1106. https://doi.org/10.1785/0120090074

Teixell, A., Arboleya, M. L., Julivert, M., and Charroud, M. (2003). Tectonic shortening and topography in the central High Atlas (Morocco). *Tectonics*, *22*(5), 1051. https://doi.org/10.1029/2002TC001460

Thurner, S., Palomeras, I., Levander, A., Carbonell, R., and Lee, C. T. (2014). Ongoing lithospheric removal in the Western Mediterranean: Evidence from Ps receiver functions and thermobarometry of Neogene basalts (PICASSO Project). *Geochem. Geophys. Geosyst.*, *15*(4), 1113–1127. https://doi.org/10.002/2013GC005124

Vajedian, S., Motagh, M., Mousavi, Z., Motaghi, K., Fielding, E. J., Akbari, B., Wetzel, H. U., and Darabi, A. (2018). Coseismic deformation field of the M_w 7.3 12 November 2017 Sarpol-e Zahab (Iran) earthquake: A decoupling horizon in the northern Zagros mountains inferred from InSAR observations. *Remote Sens.*, *10*(10), 1589. https://doi.org/10.3390/rs10101589

Vallée, M., Xie, Y. Q., Grandin, R., Villegas-Lanza, J. C., Nocquet, J. M., Vaca, S., Meng, L. S., Ampuero, J. P., Mothes, P., … Rolandone, F. (2023). Self-reactivated rupture during the 2019 M_w = 8 northern Peru intraslab earthquake. *Earth Planet. Sci. Lett.*, *601*, 117886. https://doi.org/10.1016/j.epsl.2022.117886

Wang, S., Song, C., Li, S. S., and Li, X. (2022). Resolving co- and early post-seismic slip variations of the 2021 M_w 7.4 Madoi earthquake in east Bayan Har block with a block-wide distributed deformation mode from satellite synthetic aperture radar data. *Earth Planet. Phys.*, *6*(1), 108–122. https://doi.org/10.26464/epp2022007

Wei, S. J., Ni, S. D., Chong, J. J., Zheng, Y., and Chen, Y. (2009). The 16 August 2003 Chifeng earthquake: Is it a lower crust earthquake?. *Chinese J. Geophys. (in Chinese)*, *52*(1), 111–119.

Xu, G. Y., Xu, C. J., Wen, Y. M., and Yin, Z. (2019). Coseismic and postseismic deformation of the 2016 M_W 6.2 Lampa earthquake, southern Peru, constrained by interferometric synthetic aperture radar. *J. Geophys. Res.: Solid Earth*, *124*(4), 4250–4272. https://doi.org/10.1029/2018JB016572

Xu, W. B., Dutta, R., and Jónsson, S. (2015). Identifying active faults by improving earthquake locations with InSAR data and Bayesian estimation: The 2004 Tabuk (Saudi Arabia) earthquake sequence. *Bull. Seismol. Soc. Am.*, *105*(2A), 765–775. https://doi.org/10.1785/0120140289

Xu, X. H., Sandwell, D. T., Ward, L. A., Milliner, C. W. D., Smith-Konter, B. R., Fang, P., and Bock, Y. (2020). Surface deformation associated with fractures near the 2019 Ridgecrest earthquake sequence. *Science*, *370*(6516), 605–608. https://doi.org/10.1126/science.abd1690

Xu, X. W., Wen, X. Z., Ye, J. Q., Ma, B. Q., Chen, J., Zhou, R. J., He, H. L., Tian, Q. J., He, Y. L., … An, Y. F. (2008). The M_S8.0 Wenchuan earthquake surface ruptures and its seismogenic structure. *Seismol. Geol. (in Chinese)*, *30*(3), 597–629.

Xu, Y. Y., and Wen, L. X. (2019). Relative directivity inversion of small earthquake rupture. *Geophys. J. Int.*, *218*(1), 631–639. https://doi.org/10.1093/gji/ggz179

Yang, H., Zhu, L., and Chu, R. (2009). Fault-plane determination of the 18 April 2008 Mount Carmel, Illinois, earthquake by detecting and relocating aftershocks. *Bull. Seismol. Soc. Am.*, *99*(6), 3413–3420. https://doi.org/10.1785/0120090038

Yang, Y. H., Chen, Q., Diao, X., Zhao, J. J., Xu, L., and Hu, J. C. (2021). New interpretation of the rupture process of the 2016 Taiwan Meinong M_w 6.4 earthquake based on the InSAR, 1-Hz GPS and strong motion data. *J. Geod.*, *95*(11), 121. https://doi.org/10.1007/s00190-021-01570-0

Yeck, W. L., Hatem, A. E., Goldberg, D. E., Barnhart, W. D., Jobe, J. A. T., Shelly, D. R., Villaseñor, A., Benz, H. M., and Earle, P. S. (2023). Rapid source characterization of the 2023 M_w 6.8 Al Haouz, Morocco, Earthquake. *The Seismic Record*, *3*(4), 357–366. https://doi.org/10.1785/0320230040

Zang, C., Ni, S. D., and Shen, Z. C. (2019). Rupture directivity analysis of the 2018 Hokkaido Eastern Iburi earthquake and its seismotectonic implication. *Seismol. Res. Lett.*, *90*(6), 2121–2131. https://doi.org/10.1785/0220190131

Zeyen, H., Ayarza, P., Fernàndez, M., and Rimi, A. (2005). Lithospheric structure under the western African-European plate boundary: A transect across the Atlas mountains and the Gulf of Cadiz. *Tectonics*, *24*(2), TC2001. https://doi.org/10.1029/2004TC001639

Zhang, H. J., and Thurber, C. H. (2003). Double-difference tomography: The method and its application to the Hayward Fault, California. *Bull. Seismol. Soc. Am.*, *93*(5), 1875–1889. https://doi.org/10.1785/0120020190

Zheng, Y., Ma, H. S., Lü, J., Ni, S. D., Li, Y. C., and Wei, S. J. (2009). Source mechanism of strong aftershocks (M_s≥5.6) of the 2008/05/12 Wenchuan earthquake and the implication for seismotectonics. *Sci. China Ser. D: Earth Sci.*, *52*(6), 739–753. https://doi.org/10.1007/s11430-009-0074-3

Zhu, L. P., and Helmberger, D. V. (1996). Advancement in source estimation techniques using broadband regional seismograms. *Bull. Seismol. Soc. Am.*, *86*(5), 1634–1641. https://doi.org/10.1785/BSSA0860051634

Zhu, L. P., and Ben-Zion, Y. (2013). Parametrization of general seismic potency and moment tensors for source inversion of seismic waveform data. *Geophys. J. Int.*, *194*(2), 839–843. https://doi.org/10.1093/gji/ggt137